Volume 21
Number 2
14 January 2025
Pages 159–314

Soft Matter

rsc.li/soft-matter-journal

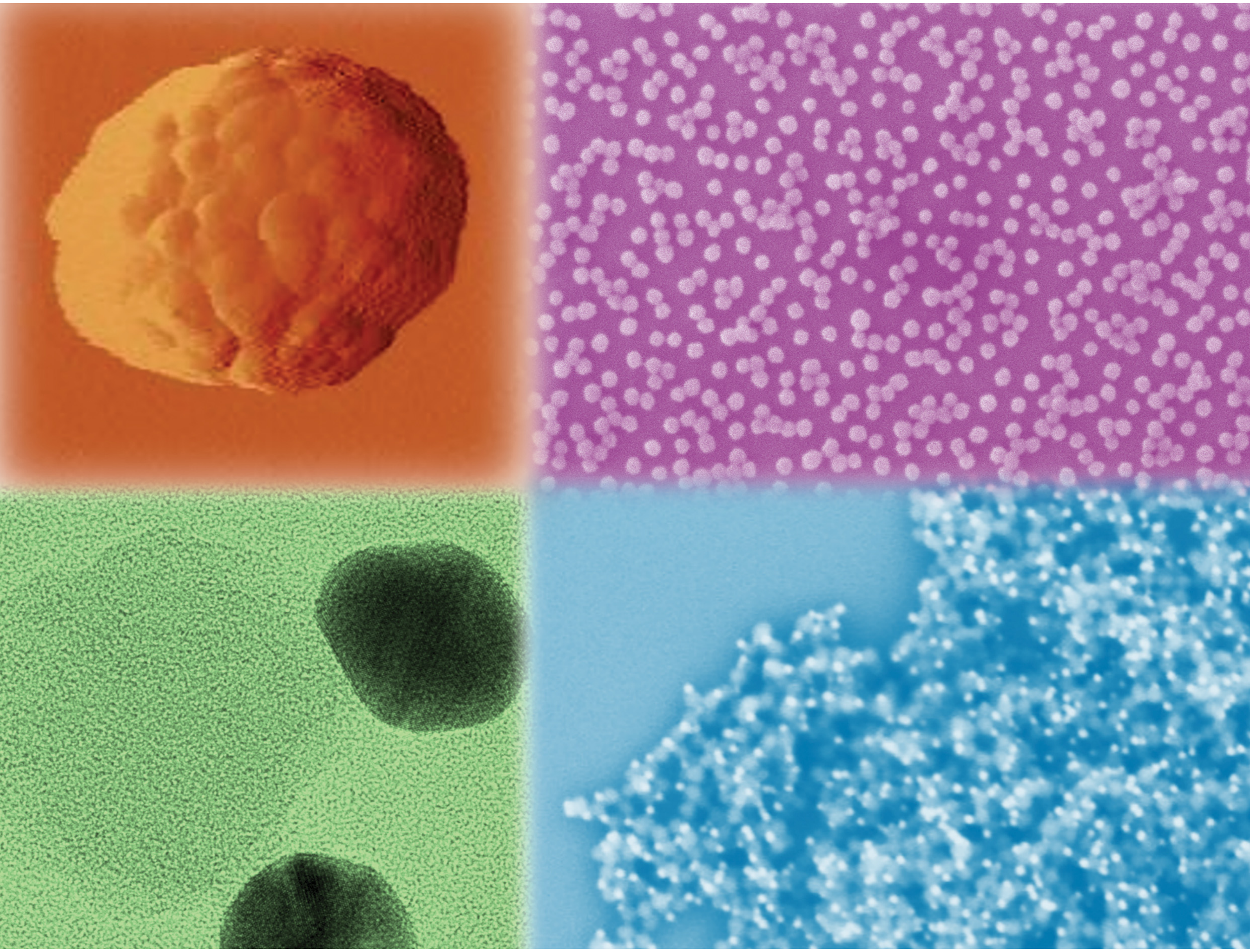

ISSN 1744-6848

ROYAL SOCIETY
OF **CHEMISTRY**

PAPER
François Baneyx *et al.*
Biomimetic mineralization of positively charged silica nanoparticles templated by thermoresponsive protein micelles: applications to electrostatic assembly of hierarchical and composite superstructures

20 YEARS
ANNIVERSARY

Soft Matter

ROYAL SOCIETY OF CHEMISTRY

PAPER

View Article Online
View Journal | View Issue

Check for updates

Cite this: *Soft Matter*, 2025, **21**, 166

Biomimetic mineralization of positively charged silica nanoparticles templated by thermoresponsive protein micelles: applications to electrostatic assembly of hierarchical and composite superstructures†

Nada Y. Naser,[a] William C. Wixson,[a] Helen Larson,[b] Brandi M. Cossairt,[b] Lilo D. Pozzo[a] and François Baneyx*[a]

Received 28th July 2024,
Accepted 30th October 2024

DOI: 10.1039/d4sm00907j

rsc.li/soft-matter-journal

High information content building blocks offer a path toward the construction of precision materials by supporting the organization and reconfiguration of organic and inorganic components through engineered functions. Here, we combine thermoresponsiveness with biomimetic mineralization by fusing the Car9 silica-binding dodecapeptide to the C-terminus of the $(VPGVG)_{54}$ elastin-like polypeptide (ELP). Using small angle X-ray scattering, we show that the short Car9 cationic block is sufficient to promote the conversion of disordered unimers into 30 nm micelles comprising about 150 proteins, 5 °C above the transition temperature of the ELP. While both species catalyze self-limiting silica precipitation, micelles template the mineralization of highly monodisperse (62 nm) nanoparticles, while unimers yield larger polydisperse species. Strikingly, and unlike traditional synthetic silica, these particles exhibit a positive surface charge, likely due to cationic Car9 sidechains projecting from their surface. Capitalizing on the high monodispersity and positive charge of the micelle-templated products, we use smaller silica and gold particles bearing a native negative charge to create a variety of superstructures *via* electrostatic co-assembly. This simple biomimetic route to positively charged silica eliminates the need for multiple precursors or surface modifications and enables the rapid creation of single-material and composite architectures in which components of different sizes or compositions are well dispersed and integrated.

Introduction

Silica-based nanomaterials have been used for decades in applications ranging from catalysis to controlled drug release, and from antimicrobial coatings to enhanced oil recovery. This broad range of uses has been driven by the low cost of silica, its thermal stability and biocompatibility, and by the fact that the material's size, morphology, and surface chemistry are all tunable.[1,2] While colloidal silica is typically synthesized at scale by liquid- (*e.g.* Stöber) or gas-phase methods,[2] more complex architectures, such as zeolites, can be accessed by macromolecular templating.[3] However, no synthetic process approaches the sophistication of diatoms which build intricately structured siliceous cell walls with extraordinary optical and physical properties by controlling silica deposition with proteins and other biomacromolecules.[4,5] In seminal work, Kröger *et al.* isolated a set of cationic peptides from the cell wall of *Cylindrotheca fusiformis* and demonstrated their role in mediating silicification under ambient conditions.[6] The so-called silaffins (for silica-affinity), and notably a constituent 19-mer peptide called R5, have been extensively studied to uncover the roles of sequence, side-chain chemistry, post-translational modifications, oligomerization, and solution conditions on silica polycondensation.[7–14]

Other peptides have also proven useful to manipulate the mineralization and organization of silica. For instance, poly(lysine) and poly(arginine) induce silica precipitation with high activity,[15] while short peptides can template more sophisticated silica structures.[16,17] Solid-binding proteins, which combine the adhesive or morphogenetic activities of guest inorganic-binding peptides with the structural or functional properties of a host protein framework, are a valuable addition to this arsenal.[18,19] For example, Car9, a silica-binding peptide of the amino acid sequence DSARGFKKPGKR,[20,21] was genetically fused to superfolder green

---

[a] Department of Chemical Engineering, University of Washington, Seattle, Washington 98195, USA. E-mail: nynaser@uw.edu, wwixson@uw.edu, dpozzo@uw.edu, baneyx@uw.edu
[b] Department of Chemistry, University of Washington, Seattle, Washington 98195, USA. E-mail: hclarson@uw.edu, cossairt@uw.edu

† Electronic supplementary information (ESI) available. See DOI: https://doi.org/10.1039/d4sm00907j

fluorescent protein (sfGFP) to study silica adhesion regimes,[22,23] print protein patterns on microscope slides,[24] and create multi-material hierarchical architectures.[25–28]

While numerous studies have established that silica-binding peptides can induce the condensation of silicic acid and modify the reaction kinetics and the morphology of the precipitated silica,[16,29] little attention has been paid to fusing these peptides to stimuli-responsive proteins to bias the outcomes of silicification. Elastin-like polypeptides (ELPs), a class of thermoresponsive intrinsically disordered proteins derived from the human tropoelastin protein, are particularly attractive for this purpose. These low-complexity proteins consist of multiple repeats of the VPGXG pentamer, where the guest residue X can be any amino acid except for proline. They exhibit lower critical solution temperature (LCST) behavior and form phase-separated droplets, or coacervates, above a characteristic transition temperature (T_t)[30,31] that can be tuned by changing the identity of the guest residue, the overall chain length, and the solution conditions (*e.g.*, pH, salt concentration, and the presence of co-solvents).[32–36] ELPs have found many uses in biomedical applications,[37–39] hierarchical self-assembly,[40–43] and inorganic nanoparticle (NP) mineralization.[44,45]

In this study, we use V54–Car9, a fusion protein between a 54-repeat of the VPGVG sequence and the Car9 silica-binding peptide, to conduct a detailed study of how temperature-driven coacervation influences silicification. We show that increasing the temperature by 5 °C above the T_t of the ELP block leads to a transition from disordered unimers to 30 nm self-assembled micelles, and that whereas both species support self-limiting silica precipitation, micelles template the mineralization of highly monodisperse 62 nm NPs while V54–Car9 unimers produce polydisperse NPs with a mean diameter of 133 nm. NPs mineralized at both temperatures exhibit a net positive charge that we attribute to the surface exposure of cationic sidechains that are not involved in the polycondensation process. We take advantage of the monodispersity and the positive charge of the silica NPs produced at high temperature for the solution-based, electrostatically driven assembly of a range of hierarchical architectures using unmodified silica and gold NPs as assembly partners.

Experimental

DNA manipulation and protein purification

An ELP template gene (Addgene) was used to produce a silica-binding ELP (V54–Car9) and a control ELP (V54) with sequences shown in Fig. 1A using standard molecular biology techniques as described in the ESI.† Plasmids were verified by sequencing and introduced into BL21(DE3) cells where proteins were purified by inverse transition cycling (Fig. S1, ESI†).[31] Protein concentrations were determined by measuring the absorbance at 205 nm and using calculated extinction coefficients[46] of 764 500 and 809 160 M^{-1} cm^{-1} for V54 and V54–Car9, respectively. Samples were stored at 4 °C until further use.

Silica mineralization

Silica mineralization reactions were conducted as described by Kröger *et al.*[6] Stock solutions of 1 M silicic acid were freshly prepared by mixing 150 μL of tetramethyl orthosilicate (TMOS, 98%, Sigma) with 850 μL of 1 mM HCl, vortexing the solution for 5 min, and rotating it for 10 min at room temperature. Aliquots (100 μL) were added to 900 μL of V54–Car9 or V54 to reach final concentrations of 100 mM silicic acid and 75 μM proteins. Solutions were immediately mixed by inverting 5 times and the reaction was allowed to progress for 8 h in water. For mineralization reactions above T_t, protein solutions were pre-incubated for 10 min in a water bath held at 45 °C prior to addition of silicic acid and the reaction was allowed to proceed for 8 h at the same temperature. Silicification products were characterized as described below. When indicated, aliquots (500 μL) were transferred to 50 kDa cutoff, 10 nm pore size, Float-A-Lyzer devices (Repligen, Waltham, MA) and were dialyzed twice against 300 mL of DI water (with stirring) for 2 h at room temperature. A final round of dialysis was conducted overnight.

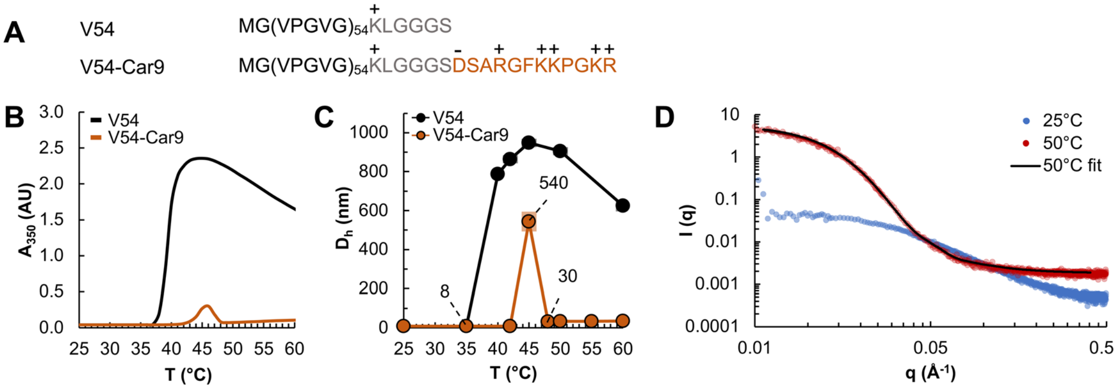

Fig. 1 The V54–Car9 silica-binding ELP transitions from unimers to 30 nm micelles above a T_t of 45 °C. (A) Amino acid sequences of the V54 control protein and V54–Car9 silica-binding ELP. The flexible linker is colored gray and the Car9 dodecapeptide is shown in orange. Positively (+) and negatively (–) charged residues are identified. Temperature-dependent evolution of turbidity (B) and hydrodynamic diameter (C) of a 75 μM solution of V54 or V54–Car9 in water when temperature was increased at a rate of 1 °C per minute. (D) Scattering intensity *versus* wave vector plots of a 710 μM solution of V54–Car9 in water below (25 °C) or above (50 °C) T_t. The high temperature data (red circles) was fitted as described in the text.

Analytical techniques

Phase transitions of the protein solutions were monitored by UV-visible spectroscopy and dynamic light scattering (DLS). For UV-visible spectroscopy, A_{350} was measured as a function of temperature on a Cary 3500 spectrophotometer equipped with a Peltier temperature controller (Agilent Technologies) using a ramp rate of 1 °C min^{-1}. Protein solutions (700 μL at a concentration of 75 μM) were blanked against DI water in semi-micro quartz cuvettes. A Zetasizer Nano ZS (Malvern) was used to measure D_h as a function of temperature. Triplicate samples (1 mL) were incubated at each temperature for 5 min before DLS measurements were acquired.

Small angle X-ray scattering (SAXS) data were collected using a Xeuss 3.0 (Xenocs) using Cu K_α radiation. To achieve sufficient scattering signal for the experiments in Fig. 1D, protein solutions were subjected to two cycles of concentration using Microcon centrifugal filtration units with a 10 kDa cutoff (Millipore) to reach a final concentration of 17 mg mL^{-1} (710 μM). Mineralization products were characterized by SAXS as produced. Samples were loaded into 1.5 mm quartz capillaries (Charles Supper), sealed with epoxy, and placed under vacuum in a Peltier temperature-controlled stage. To improve the signal-to-noise ratio observed in the protein samples at 25 °C, they were measured in a flow through cell unit (BioCUBE). All samples were exposed four times at varying detector distances.

Scattering data was processed with the XSACT software (Xenocs) by azimuthally averaging 2D scattering images to produce 1D scattering profiles. Water backgrounds were subtracted and 1D profiles from different detector distances were merged. Radii of gyration were calculated by Guinier analysis (Fig. S3B, ESI†). Model fitting was performed in the SASView software. Data from the protein solutions at 45 °C were fit to the spherical block copolymer micelle model developed by Pedersen.[47] Data from mineralization products were fit to a spherical raspberry model[48] assuming a polydisperse core particle of radius R_c with monodisperse small particles on the periphery of radius R_p. Further, it was assumed the core and periphery possess equivalent scattering length densities and that the penetration depth ratio was zero (*i.e.*, all small particles on the periphery expose a hemisphere to their surroundings).

For scanning electron microscopy (SEM), samples were diluted 100-fold in DI water, and aliquots (5 μL) were deposited on silicon wafers that were allowed to air dry overnight. For mineralization reactions above T_t, samples were diluted 100-fold in DI water pre-heated to 45 °C, deposited on pre-heated silicon wafers, and allowed to air dry overnight in an incubator held at the same temperature. Images were acquired on an Apreo-S SEM (Thermo Scientific) operated at 2 kV and 13 pA.

For transmission electron microscopy (TEM), samples were diluted 10-fold in DI water. Aliquots (10 μL) were deposited on carbon-coated copper grids (Electron Microscopy Sciences and Ted Pella) and allowed to sit for 5 min before excess solution was wicked out with a laboratory tissue. Images were acquired on a Tecnai F20 SuperTwin TEM (FEI) at an acceleration voltage of 200 kV and analyzed using ImageJ (NIH).

For atomic force microscopy (AFM), aliquots (10 μL) of samples were deposited onto freshly cleaved mica substrates (Ted Pella). After 5 minutes, excess water was wicked out with laboratory tissue and samples were further dried by evaporation. AFM images were captured in the dry state using the tapping mode on an ICON AFM (Bruker) and Multi75AI-G probes. Offline AFM data processing was performed using Gwyddion software.[49]

Thermogravimetric analysis (TGA) was conducted on lyophilized mineralization products that had been extensively dialyzed to remove free and loosely bound proteins. Experiments were performed in a Q50 TGA instrument (TA Instruments). Lyophilized powder was loaded into an alumina crucible on platinum tray and heated to 800 °C at a ramp rate of 20 °C per minute in air (100 mL min^{-1}).

Results

The V54–Car9 solid-binding ELP forms micelles above its transition temperature

To combine the mineralization properties of a solid-binding peptide with the thermoresponsive phase segregation behavior of an ELP, we fused the sequence encoding the Car9 dodecapeptide (DSARGFKKPGKR) to the C-terminus of a 54-repeat of the VPGVG sequence *via* a flexible KLGGGS linker (Fig. 1A). A control protein lacking the Car9 dodecapeptide (denoted V54) exhibited characteristic LCST behavior[30,31] with a sharp increase in both the absorbance at 350 nm (A_{350}) and the hydrodynamic diameter (D_h) as the temperature exceeded a T_t of 40 °C (Fig. 1B and C, black traces). In contrast, the V54–Car9 fusion protein only experienced a transient peak in turbidity between 42 and 48 °C before reaching a slightly higher value as the temperature increased (Fig. 1B, orange trace). Results were well explained by DLS measurements showing that the D_h of V54–Car9 increased from 8 to 540 nm between 42 and 45 °C before declining to about 30 nm over the next 2–3 °C (Fig. 1C, orange trace). To gain insights on kinetics, we monitored the D_h at 65 °C, a temperature that far exceeds its T_t ($\sim$45 °C). Within two minutes, V54–Car9 molecules transitioned from unimers to intermediate aggregates ranging in size from 200 to 300 nm (Fig. S2, ESI†). These species progressively disappeared after 3 minutes to the profit of a peak centered at a D_h of 30 nm.

Similar phase transitions have been reported for amphiphilic block copolymers,[50–55] including those consisting of a hydrophobic ELP block (where the guest residue is V) fused to a hydrophilic ELP block (where the guest residue is G, A, or S). For such diblock ELPs, a temperature increase above the T_t of the hydrophobic block leads to the formation of spherical micelles displaying the hydrophilic block on their exterior.[56–62] This feature was exploited by Lopez and coworkers to display the 19-residue long R5 peptide on the surface of 50 nm micelles by fusing it to a 300-residue long hydrophilic block that was itself fused to a 300-residue long hydrophobic block.[41,44]

We used SAXS to determine if V54–Car9 adopted a similar micellar structure above 45 °C despite lacking a long hydrophilic ELP block. At 25 °C, the SAXS profile of V54–Car9 was consistent with that of polymeric random coils and intrinsically disordered proteins (Fig. 1D, blue symbols; also see Fig. S3A, ESI†). This observation is consistent with the fact that ELPs are predominantly random coils below T_t,[63] and that the Car9 peptide adopts a range of conformations in solution and at interfaces rather than folding into a well-defined structure.[23] Above T_t, the SAXS profile was consistent with spherical particles with a mean radius of gyration (R_g) of 13 nm, as determined by Guinier analysis (Fig. 1D, red symbols, and Fig. S3B, ESI†). Fitting to a more sophisticated polymer micelle model[47] allowed high-fidelity capture of the high temperature data (Fig. 1D, black curve). The analysis revealed that 140 ± 9 V54–Car9 molecules self-assemble to form a micelle with a 15 ± 0.2 nm core radius that is consistent with the D_h of 30 nm determined by DLS. The structural transition was made more obvious by a Kratky plot of the SAXS profiles, in which the characteristic plateau of an intrinsically disordered protein at 25 °C gave rise to the bell-like profile of a polymer micelle above T_t (Fig. S3A, ESI†).[64,65] Consistent with a structure in which a coacervated V54 core is surrounded by cationic Car9 extensions, the ζ potential of the micelles was +19 ± 3 mV (Table 1). In summary, the short Car9 peptide is sufficient to impart diblock behavior to a 54-repeat hydrophobic ELP, driving the formation of micelles at a T_t that is about 5 °C higher than that of the ELP block.

Silicification above T_t yields highly monodisperse silica nanoparticles

To determine how temperature-induced micellization would influence silica precipitation outcomes, solutions of V54–Car9 in water were heated to 45 °C, supplemented with an excess of silicic acid, and the silicification reaction was allowed to progress at 45 °C for 8 h (hot synthesis). D_h was measured at intermediate times to monitor particle growth. An increase in turbidity correlating with an increase in D_h (∼62 nm) was observed within 30 min, with no further evolution over time (Fig. S4, red trace, ESI†). SEM (Fig. 2B) and TEM (Fig. 2C and Fig. S5, ESI†) revealed the production of monodisperse NPs with an average diameter of 56 ± 4 nm (N = 100) under dry conditions. Repeating the silicification experiment at 22 °C (cold synthesis) led to the formation of larger particles (D = 96 ± 16 nm under dry conditions) exhibiting a higher degree of polydispersity, and to the production of occasional aggregates (Fig. 2A and Fig. S4, blue trace, ESI†). Consistent with imaging results, polydispersity index (PDI) values from DLS measurements (Fig. 2D) were 0.03 and 0.12 for the products of hot and cold synthesis, respectively. In the absence of the Car9 extension, and irrespective of the reaction temperature, the V54 ELP induced the precipitation of silica particles of random sizes and shapes (Fig. S6, ESI†). Further, only a few large silica structures were observed when silicic acid was added to water in the absence of protein (Fig. S7, ESI†).

The SAXS profiles of both synthesis products were consistent with spherical particles. They also exhibited a turnover at high q-values that is indicative of small surface features (Fig. 3A). We therefore used a spherical raspberry model[48] instead of a simpler sphere model to fit the scattering data. This analysis confirmed that the hot synthesis products are highly monodisperse silica spheres with a mean core diameter of 55 ± 3 nm and a PDI of 0.12 (Fig. 3B, red). The turnover in scattering was successfully modelled as uniform projecting hemispheres that were 2 ± 0.2 nm in diameter (Fig. 3C). On the other hand, the scattering profile of the cold synthesis products (Fig. 3A, blue) lacked strong secondary peaks and had a steep negative slope at low q-values, which is indicative of polydispersity. Indeed, the fitting procedure revealed particles with a mean core diameter of 116 nm, a larger PDI of 0.18, and surface features that could be modelled as hemispheres 1.6 ± 0.4 nm in diameter (Fig. 3B, blue). We confirmed that protrusions were present on the surface of both particles using tapping-mode AFM and high-resolution transmission electron microscopy (HRTEM) shown in Fig. 3D–I. In agreement with the SAXS data, these nodules were more uniform and regularly distributed on the surface of hot synthesis products (Fig. 3D–F). With a diameter of ∼3 nm determined from TEM data and ∼2 nm from SAXS data fitting, these small particles likely correspond to the primary units that make up biomimetic silica structures.[9]

Templated silicification is self-limiting and produces positively charged nanoparticles

Several scenarios can account for the formation of silica particles of defined sizes including exhaustion of the silicic acid precursor, termination of growth by capping, and self-limiting growth. With an over 1300-fold molar excess of silicic acid to proteins, the first possibility appeared unlikely. Indeed, when both cold and hot synthesis products were supplemented with additional V54–Car9 at room temperature after the initial mineralization reaction, we observed additional silica precipitation, indicating that free silicic acid remains available in solution despite the observed cessation of nanoparticle growth (Fig. 4C and D). However, and unlike in the cold synthesis case, the products of the reaction were micrometer sized silica islands that grew around the pre-mineralized nanoparticles

Table 1 Summarizing the silicification reaction conditions and characterization of mineralized silica NPs

$[Si(OH)_4]$ (mM)	Reaction temp. (°C)	Reaction time (h)	D_h DLS (nm)	D SEM (nm)	R_g SAXS (nm)	D_{sphere}[a] (nm)	ζ potential (mV)
0	22	N.A.	8 ± 1	N.A.	5	N.A.	8 ± 5
0	45	N.A.	31 ± 8	N.A.	13	34	19 ± 3
100	22	8	133 ± 32	96 ± 16	49	127	38 ± 0.4
100	45	8	62 ± 10	56 ± 4	24	62	39 ± 0.1

[a] D_{sphere} was calculated based on R_g using the relationship: $D_{sphere} = 2 \times \sqrt{\frac{5}{3}}R_g$.[66] N.A. = not applicable.

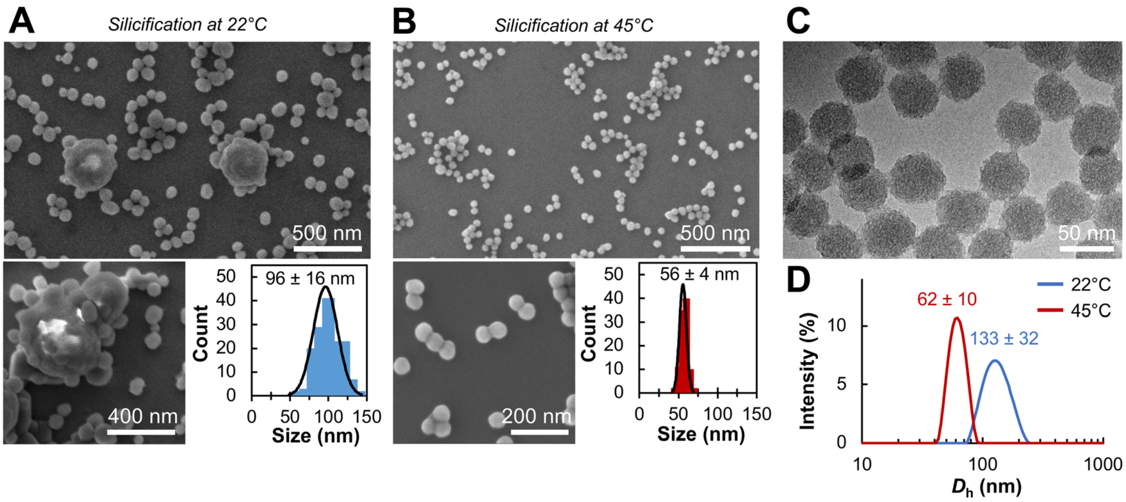

Fig. 2 Silicification above T_t yields highly monodisperse nanoparticles. (A) Field of view (top) and magnified (bottom left) SEM images of mineralization products obtained at 22 °C along with their size distribution (bottom right). (B) As in panel (A) except that the mineralization reaction was conducted at 45 °C. (C) Representative TEM image of the 45 °C mineralization products. (D) DLS intensity profiles of mineralization products obtained at 22 °C or 45 °C. All experiments were conducted at the indicated temperatures and in water using 75 μM of V54–Car9 and 100 mM of silicic acid.

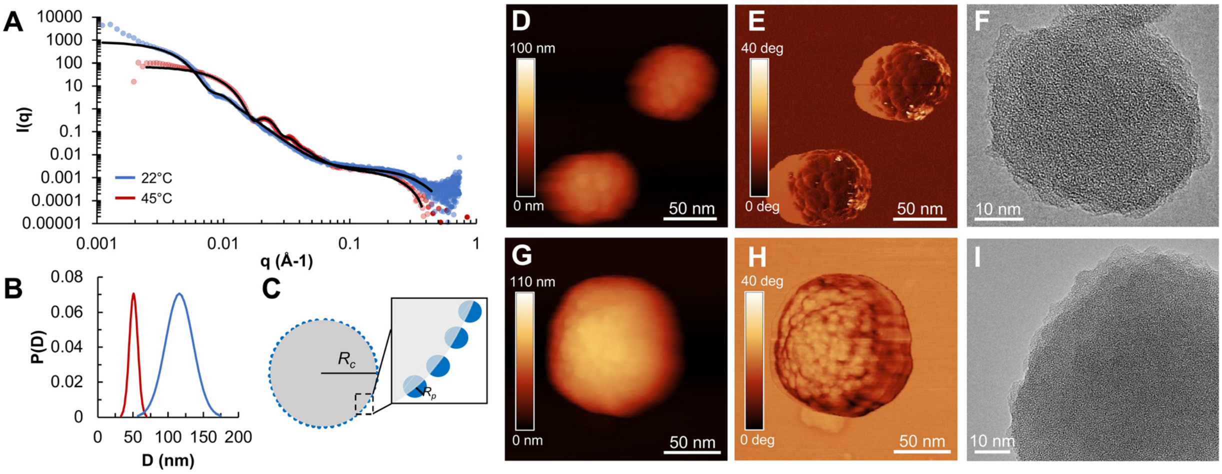

Fig. 3 SAXS, AFM, and HRTEM characterization of silicification products. (A) SAXS profiles of silicification products obtained at 22 °C (blue) or 45 °C (red) fit to a raspberry sphere model (solid lines), (B) distribution of core particle diameter from SAXS fit. (C) Schematic representation of the raspberry structure used for fitting of SAXS profiles. The core particles with radius R_c are decorated with embedded spheres of radius R_p, each with a projecting hemisphere. Tapping-mode AFM topography images (D) and (G), phase images (E) and (H), and HRTEM images (F) and (I) of NPs mineralized at 45 °C or 22 °C, respectively.

and likely did not form silane bonds with them (Fig. 3C, yellow arrow). We attribute this result to a slower growth of the silica matrix due to depletion of the precursor in the initial mineralization phase and concomitant diffusion limitations.

Consistent with a unique surface chemistry, our templated NPs exhibited a positive ζ potential of about 40 mV (Table 1) as well as long-term colloidal stability following extensive dialysis against water and storage at 4 °C. X-ray photoelectron spectroscopy (XPS) of the oxygen and nitrogen signals confirmed the presence of organics at, or within the first ∼10 nm of the surface (Fig. S8, ESI†). This result was quite unexpected, as protein and peptide inducers of silicification typically become fully encased within the growing silica matrix, leading to a negative ζ potential.[3,8,67]

To rationalize the positive ζ potential displayed by the mineralized silica, we conducted a series of experiments to determine if V54–Car9 unimers were merely bound to the particles' surface or if they were partially embedded within the silica matrix, allowing cationic sidechains to emanate from the particles' surface. First, extensively dialyzing the nanoparticle solution against water did not change the ζ potential over the course of seven days, reflecting strong surface interactions or the integration of the proteins within the particles. Second, and in contrast with our recent results with ELP-decorated AuNPs,[68] neither the cold nor the hot synthesis products experienced an increase in D_h when the solution temperature was raised to 55 °C to induce colloidal aggregation *via* coacervation of any surface exposed

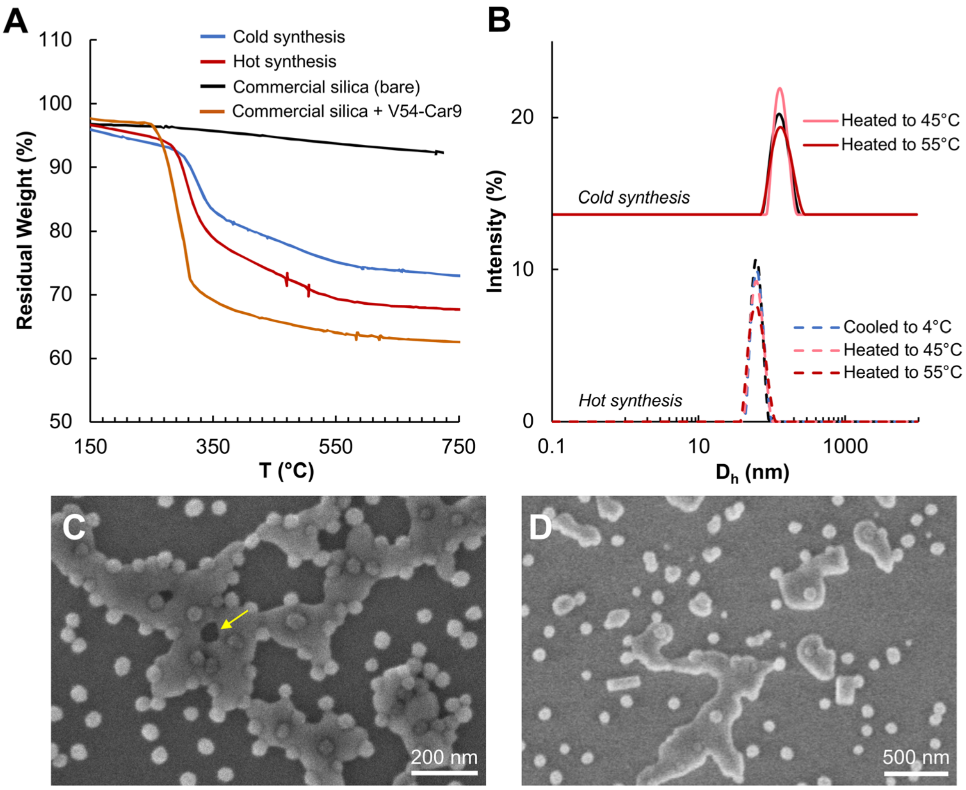

Fig. 4 (A) TGA thermograms of hot (red) and cold (blue) synthesis products compared to commercial silica before (black) and after (orange) decoration with a molar excess of V54–Car9. All TGA samples were extensively dialyzed to remove loosely bound or unreacted ligands. (B) DLS intensity profiles of silicification products at 22 °C (solid lines) or 45 °C (dashed lines) after incubation at the indicated temperatures for 10 min each. SEM images of mineralized nanoparticles at 45 °C (C) or 22 °C (D) after the addition of 75 μM V54–Car9 and incubation for 10 min.

ELPs (Fig. 4B). This finding strongly suggests that the ELP segments are embedded within the silica matrix rather than being available at the surface of the particles. Finally, TGA of 65 nm commercial silica nanoparticles that had been decorated with V54–Car9 revealed an onset of organic pyrolysis at about 250 °C (Fig. 4A, orange trace). This temperature increased to 290 °C for the hot synthesis and 300 °C for the cold synthesis products, reflecting not only a more intimate integration of the proteins within the silica matrix, but also subtle differences in the nature of the interaction between the two types of nanoparticles.

Using positively charged silica for the co-assembly of silica and composite superstructures

We exploited the fact that nanoparticles mineralized under hot synthesis conditions are both positively charged and highly uniform in size to create colloidal assemblies through electrostatic interactions with unmodified NPs bearing an intrinsic net negative charge. In a first demonstration, we mixed the mineralized particles with an excess of commercial, 10 nm silica NPs (Fig. 5A, step 1). This operation led to the decoration of the mineralized particles' surface with the smaller silica nanospheres and neutralized the ζ potential (Fig. 5B). In the resulting raspberry architecture, the 10 nm nanospheres were rather evenly separated from each other, as would be expected if they were experiencing a balance of attractive electrostatic interactions with discrete, positively charged regions of the mineralized particles, and electrostatic repulsion with each other. When an excess of mineralized nanoparticles was added to the product of the first assembly step (Fig. 5A, step 2), SEM imaging revealed quantitative depletion of the 10 nm nanoparticles accompanied by the formation of an open, extended, and fractal-like networks, in which positively charged particles are connected to one another by the smaller silica nanospheres (Fig. 5C).

To demonstrate that different architectures can be accessed by manipulating the size of the unmodified silica NPs (Fig. 6A), we mixed the mineralized NPs with 20 nm commercial silica nanospheres. When the 20 nm particles were used at high concentrations (5–10 mg mL^{-1}), the mixture was colloidally stable and exhibited an overall negative ζ potential. Reducing the concentration 10-fold (to 0.5 mg mL^{-1} or about 75 μM) led to the formation of a white flocculate after overnight incubation at room temperature. SEM imaging revealed that this material consisted of rather tightly packed, multilayer aggregates of the two components (Fig. 6B) in which mineralized nanoparticles are interconnected by smaller, and oppositely charged silica nanospheres (Fig. 6B inset, yellow arrows).

We extended the approach to the production of a composite superstructure by mixing unmodified, 20 nm gold nanoparticles (AuNPs) with the mineralized silica. Overnight incubation at the molar ratio used in the experiment of Fig. 6B led to the formation of a very similar architecture with bridging AuNPs well dispersed in the material (Fig. 6C and inset of Fig. 6D). These structures were stable for at least six months (Fig. S10, ESI†). Finally, and consistent

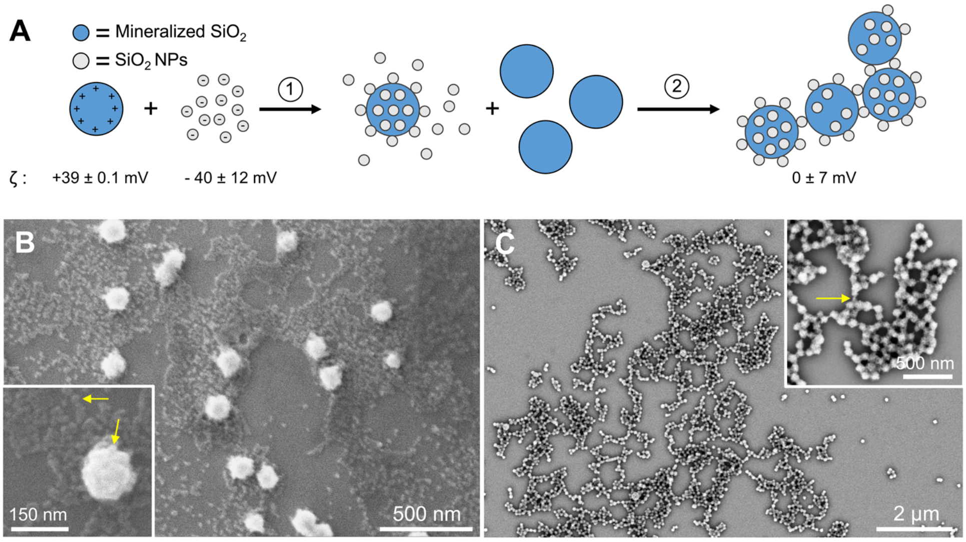

Fig. 5 (A) Schematic of the electrostatically driven co-assembly of positively charged mineralized silica NPs (blue) with an excess of 10 nm negatively charged silica NPs (gray). (B) Products of assembly step (1). (C) Products of assembly step (2).

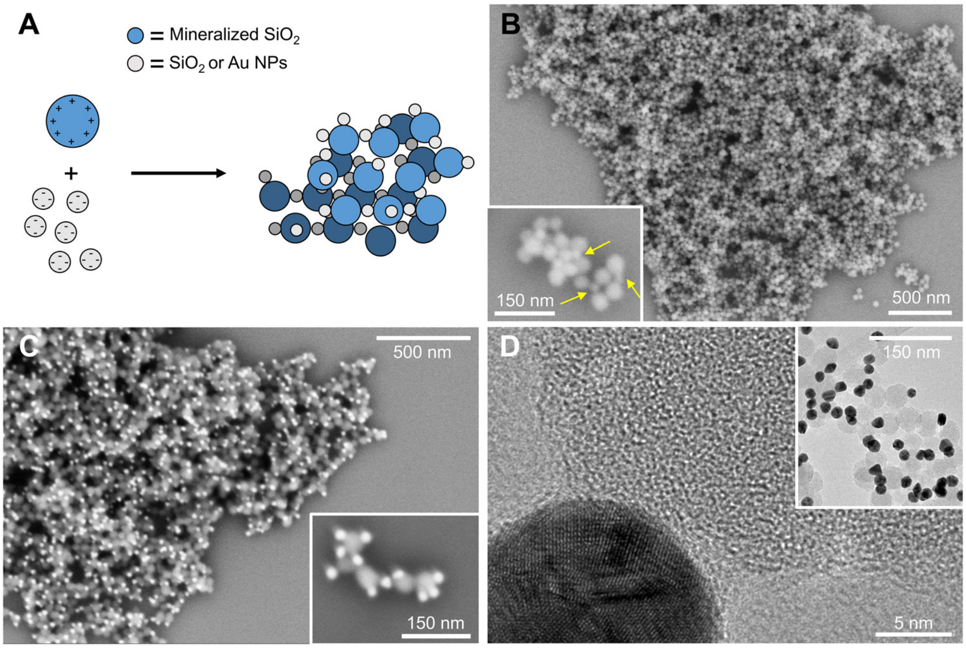

Fig. 6 (A) Schematic of electrostatically driven co-assembly of positively charged mineralized silica NPs (blue) and 20 nm negatively charged NPs (gray). SEM images and magnified insets of the co-assembly of mineralized NPs with 20 nm silica NP (B) or 20 nm AuNPs (C). (D) HRTEM of the silica–Au interface with field of view inset.

with the lack of an adsorbed protein shell, HRTEM imaging showed an intimate interaction between the amorphous mineralized silica and the crystalline AuNPs (Fig. 6D).

Discussion

Micelle formation by V54–Car9

Amphiphilic diblock copolymers have been extensively studied both theoretically[69–71] and experimentally[72,73] for their ability to self-assemble into a range of micellar structures,[74] with recent work focusing on combining the thermoresponsive properties of ELPs with diblock copolymer behavior to create temperature-responsive micelles.[60] In these applications, a hydrophobic ELP block (*i.e.*, one that contains a hydrophobic guest residue such as V) is connected to a moderately hydrophilic block (*e.g.*, an ELP with charged[59] or neutral[44] guest residues) or to a protein or a polymer[75,76] to create a construct with reversible thermoresponsive micellization behavior. In most cases, the hydrophilic block needs to be at least half as long as the hydrophobic block to form sub-100 nm micelles. For the first time, we show that such long hydrophilic blocks are not required for micelle formation since the Car9 dodecapeptide is sufficient to confer diblock behavior to the V54 ELP despite representing less than 5% of the V54–Car9 amino acid sequence. Micellization arises 5 °C above the T_t of the ELP block in a process that involves the formation of intermediate aggregates 200 to 300 nm in size, and their subsequent resolution into highly monodisperse equilibrium structures that are 30 nm in diameter and comprise about 140 ELPs. This configuration provides about 20 nm^2 of surface area for the organization of a Car9 segment on the micelle's exterior. Since Car9 can adopt a variety of conformations,[23] each core-tethered peptide must optimize the orientation of its sidechains to minimize destabilizing interactions with all its nearest neighbors. Considering that five of the 12 residues that make up Car9 are positively charged, this operation should lead to the presentation of a high density of basic side chains to the solvent, consistent with the appreciable ζ potential of approximately +20 mV. Whether the five basic residues of Car9 are necessary and sufficient to induce the formation of a well-behaved corona around the coacervated ELP core, and their role in this process, is currently being investigated.

Silicification by V54–Car9 micelles and unimers

The ability of V54–Car9 micelles to template the formation of highly monodisperse silica NPs when mixed with a solution of silicic acid in the absence of a buffer was not entirely unexpected. Han *et al.* previously reported that ELP$_{\text{Diblock}}$-R5, an amphiphilic ELP consisting of 60 repeats of the hydrophobic (GVGVP) sequence and 30 repeats of the hydrophilic (GAGVPGGGVP) sequence followed by the silaffin-derived R5 peptide (SSKKSGSYSGSKGSKRRIL), formed 50 nm micelles above a T_t of 33 °C. When supplemented with silicic acid, these micelles templated the formation of silica NPs at 37 °C.[44] However, there are two important differences between the results of this study and ours. First, the particles synthesized by Han and coworkers exhibited a negative ζ potential (−27 mV), indicating that the positively charged micelles were fully encapsulated in a mineral terminated by negatively charged silanol groups. Second, no silica precipitation was observed when silicic acid was added to dispersed ELP$_{\text{Diblock}}$-R5 unimers at 25 °C.

Like ELP$_{\text{Diblock}}$-R5 micelles, V54–Car9 micelles are likely to serve as nucleation and growth centers for silica polycondensation by displaying a high density of positively charged amino acids on their coronae. By analogy with a mechanism suggested for polyamine-mediated silicification,[77] we propose that the adsorption of silica monomers (or small oligomers) onto the amino groups of vicinal cationic side chains of Car9 promotes condensation reactions by bringing the inorganic species in proximity. This process leads to the formation of larger oligomers that grow into 1–3 nm particles.[9,78] These primary particles, which eventually come into contact and become linked by siloxane bonds, may be responsible for the surface features modelled by SAXS fitting and the granularity visualized in the TEM and AFM experiments in Fig. 3.

If similar silicification mechanisms are at play, why do ELP$_{\text{Diblock}}$-R5 micelles produce negatively charged silica particles while V54–Car9 micelles yield positively charged ones? A major difference between the two systems is that a 300-residue long hydrophilic block is present between the hydrophobic ELP block and the silica-binding peptide in ELP$_{\text{Diblock}}$-R5, relative to a six amino acids long linker in V54–Car9. Thus, R5 should experience considerably more degrees of freedom than Car9, which would facilitate interactions between primary particles and promote the encapsulation of the entire micelle. We propose that the lower mobility of coronal Car9 peptides and a stronger structural correlation with their neighbors introduces inwards directionality in the silica growth process that precludes complete encapsulation of the peptide. Using molecular dynamics (MD) simulations, we previously reported that three of Car9's basic residues (Arg-4, Lys-7, and Lys-8, starting the numbering with the first residue) spend significant more time on silica surfaces relative to Lys-11 and Arg-12.[23] If a longer residence time on silica is indicative of a more active participation in the silicification process, the positive charge of mineralized V54–Car9 micelles could be due to the side chains of Lys-11 and/or Arg-12 emanating from the surface of the mineralized silica.

Why do ELP$_{\text{Diblock}}$-R5 unimers not induce nanoparticle formation below T_t[44] while V54–Car9 unimers are effective at this task is well explained by the fact that Car9 is a better catalyst of silicification in water and phosphate-free buffers. Extensive literature indicates that the formation of R5 oligomers through the bridging action of phosphate ions[8,79] (or the post-translational phosphorylation of the peptide's serine residues)[80] significantly improves its silica precipitation ability. Additionally, a direct comparison of the ability of genetic fusions between green fluorescent protein (GFP) and the R5 or Car9 sequences revealed that whereas GFP-Car9 readily precipitated titania from the alkoxide-like precursor TiBALDH in mildly acidified citrate buffer, GFP-R5 was unable to do so.[81] A more interesting question is why do the NPs formed by V54–Car9 unimers under cold synthesis conditions also exhibit a positive ζ potential. We believe that this result is explained, at least in part, by the ability of Car9 to form oligomers when its Arg-4, Lys-7, and Lys-8 anchor residues are engaged with silica.[23] While less efficient at templating the mineralization of uniform particles than V54–Car9 micelles, these small oligomers could still impart directionality to the silicification reaction, precluding encapsulation within the silica matrix and leading to the production of spherical particles that project cationic sidechains.

Electrostatic assembly of hierarchical architectures

Silica nanostructures exhibiting a positive surface charge have proven valuable for catalysis[82,83] and biomedical applications,[84–86] including controlled encapsulation and release of anionic drugs, surface decoration with DNA, efficient penetration of cell membranes, and electrostatically-driven binding to negatively-charged cancer cells.[87] Reversal of the silica particles' native negative charge is usually achieved by adsorption of positively charged species or by chemical modification of the surface silanol groups

(Si–OH) with cationic ligands. Unfortunately, these strategies often result in high polydispersity, poor colloidal stability, and/or silica dissolution.[87,88] Here, we described a simple approach to produce highly uniform positively charged silica nanospheres that exhibit exceptional colloidal stability and can be fabricated biomimetically under mild conditions without a need for multiple precursors, or post-synthesis surface modifications.[84,87]

These ready-to-use NPs were exploited to create 2- and 3-dimensional superstructures *via* electrostatically driven co-assembly with negatively charged NPs. From raspberry and fractal structures to more tightly packed composites, we achieved a broad range of architectures by changing the diameter, concentration, and composition of the anionic components. Although these proof-of-concept superstructures were obtained with little optimization and without annealing, we observed not only a rather uniform distribution of the two types of NPs in the final assemblies, but also the formation of intimate contacts between gold and silica components. This feature may be particularly valuable for the design of efficient catalytic and photoelectronic structures that exhibit high sensitivity to interfacial separation.[27,83,89,90]

Conclusion

We have shown that while a control ELP lacking a silica-binding extension undergoes hydrophobic collapse into micron-size coacervates above its T_t, the V54–Car9 silica-binding ELP self-assembles into 30 nm micelles displaying Car9 on their exterior, establishing that a short cationic peptide can impart diblock behavior to a large hydrophobic ELP. We exploited these micelles to template the mineralization of highly uniform, positively charged silica NPs under mild conditions. Multimodal characterization of micellization kinetics and mineralization products provided insights into the self-limiting reaction and revealed nanoscale surface texture. Finally, we exploited the positive charge and monodispersity of NPs silicified at high temperature for the electrostatically driven, one-step assembly of hierarchical architectures, accessing a range of superstructures by modifying the size and composition of the negatively charged co-assembly partner. We anticipate that it will be possible to mineralize particles of different sizes, morphologies, and compositions by changing the sequence and length of the solid-binding segment and ELP block. Whether these particles will retain a positive charge remains to be determined, but if they do, they will enrich the range of architectures that can be produced by electrostatic co-assembly. This simple biomimetic approach to the synthesis of colloidally stable, positively charged silica NPs and hierarchical and composite superstructures should prove useful for a broad range of applications including carriers for triggered anticancer drug release,[91] stabilizing agents for nuclear decontamination,[92] and solid supports for carbon monoxide oxidation.[93–96]

Data availability

The data supporting this article have been included as part of the ESI.†

Conflicts of interest

The authors declare the following competing financial interest(s): F. B. declares a competing financial interest in Proteios Technology, Inc., which researches and commercializes Car9-based technologies.

Acknowledgements

We would like to thank Jinrong Ma and Zhixing Lin for their assistance with molecular biology and characterization. This material was based upon work supported by the US Department of Energy, Office of Science, Office of Basic Energy Sciences, as part of the Energy Frontier Research Centers program: CSSAS – The Center for the Science of Synthesis Across Scales under Award Number DE-SC0019288. Part of this work was conducted at the Molecular Analysis Facility, a National Nanotechnology Coordinated Infrastructure (NNCI) site at the University of Washington, which is supported in part by funds from the National Science Foundation (awards NNCI-2025489, NNCI-1542101), the Molecular Engineering & Sciences Institute, and the Clean Energy Institute. Part of this work was conducted using instrumentation funded by the University of Washington Student Technology Fee. This work benefited from the use of the SasView application, originally developed under NSF award DMR-0520547. SasView contains code developed with funding from the European Union's Horizon 2020 research and innovation programme under the SINE2020 project, grant agreement no. 654000. The authors acknowledge the use of facilities and instrumentation supported by the U.S. National Science Foundation through the use of the Major Research Instrumentation (MRI) program (DMR-2116265) and the UW Molecular Engineering Materials Center (MEM-C), a Materials Research Science and Engineering Center (DMR-2308979).

References

1 R. Ciriminna, A. Fidalgo, V. Pandarus, F. Béland, L. M. Ilharco and M. Pagliaro, The Sol–Gel Route to Advanced Silica-Based Materials and Recent Applications, *Chem. Rev.*, 2013, **113**(8), 6592–6620, DOI: 10.1021/cr300399c.

2 E. Hyde, A. Seyfaee, F. Neville and R. Moreno-Atanasio, Colloidal Silica Particle Synthesis and Future Industrial Manufacturing Pathways: A Review, *Ind. Eng. Chem. Res.*, 2016, **55**(33), 8891–8913, DOI: 10.1021/acs.iecr.6b01839.

3 M. A. A. Abdelhamid and S. P. Pack, Biomimetic and bioinspired silicifications: Recent advances for biomaterial design and applications, *Acta Biomater.*, 2021, **120**, 38–56.

4 M. Hildebrand, Diatoms, biomineralization processes, and genomics, *Chem. Rev.*, 2008, **108**(11), 4855–4874.

5 C. Heintze, P. Formanek, D. Pohl, J. Hauptstein, B. Rellinghaus and N. Kröger, An intimate view into the silica deposition vesicles of diatoms, *BMC Mater.*, 2020, **2**(1), 1–15, DOI: 10.1186/s42833-020-00017-8.

6 N. Kröger, R. Deutzmann and M. Sumper, Polycationic peptides from diatom biosilica that direct silica nanosphere formation, *Science*, 1999, **286**(5442), 1129–1132.

7 N. Kröger, R. Deutzmann, C. Bergsdorf and M. Sumper, Species-specific polyamines from diatoms control silica morphology, *Proc. Natl. Acad. Sci. U. S. A.*, 2000, **97**(26), 14133–14138.
8 M. R. Knecht and D. W. Wright, Functional analysis of the biomimetic silica precipitating activity of the R5 peptide from Cylindrotheca fusiformis, *Chem. Commun.*, 2003, (24), 3038–3039.
9 D. J. Belton, O. Deschaume and C. C. Perry, An overview of the fundamentals of the chemistry of silica with relevance to biosilicification and technological advances, *FEBS J.*, 2012, **279**(10), 1710–1720.
10 C. C. Lechner and C. F. W. Becker, A sequence-function analysis of the silica precipitating silaffin R5 peptide, *J. Pept. Sci.*, 2014, **20**(2), 152–158.
11 C. C. Lechner and C. F. W. Becker, Silaffins in silica biomineralization and biomimetic silica precipitation, *Mar. Drugs*, 2015, **13**(8), 5297–5333.
12 M. Sumper, S. Lorenz and E. Brunner, Biomimetic Control of Size in the Polyamine-Directed Formation of Silica Nanospheres, *Angew. Chem., Int. Ed.*, 2003, **42**(42), 5192–5195.
13 L. Senior, M. P. Crump, C. Williams, P. J. Booth, S. Mann and A. W. Perriman, *et al.*, Structure and function of the silicifying peptide R5, *J. Mater. Chem. B*, 2015, **3**(13), 2607–2614.
14 P. J. Lopez, C. Gautier, J. Livage and T. Coradin, Mimicking Biogenic Silica Nanostructures Formation, *Curr. Nanosci.*, 2005, **1**, 73–83.
15 T. Coradin, O. Durupthy and J. Livage, Interactions of amino-containing peptides with sodium silicate and colloidal silica: A biomimetic approach of silicification, *Langmuir*, 2002, **18**(6), 2331–2336.
16 M. B. Dickerson, K. H. Sandhage and R. R. Naik, Protein- and peptide-directed syntheses of inorganic materials, *Chem. Rev.*, 2008, **108**(11), 4935–4978.
17 M. J. Limo, A. Sola-Rabada, E. Boix, V. Thota, Z. C. Westcott and V. Puddu, *et al.*, Interactions between Metal Oxides and Biomolecules: from Fundamental Understanding to Applications, *Chem. Rev.*, 2018, **118**(22), 11118–11193, DOI: **10.1021/acs.chemrev.7b00660**.
18 K. Pushpavanam, J. Ma, Y. Cai, N. Y. Naser and F. Baneyx, Solid-Binding Proteins: Bridging Synthesis, Assembly, and Function in Hybrid and Hierarchical Materials Fabrication, *Annu. Rev. Chem. Biomol. Eng.*, 2021, **12**(1), 333–357, DOI: **10.1146/annurev-chembioeng-102020-015923**.
19 C. L. Chen and N. L. Rosi, Peptide-Based Methods for the Preparation of Nanostructured Inorganic Materials, *Angew. Chem., Int. Ed.*, 2010, **49**(11), 1924–1942, DOI: **10.1002/anie.200903572**.
20 B. L. Coyle and F. Baneyx, A cleavable silica-binding affinity tag for rapid and inexpensive protein purification, *Biotechnol. Bioeng.*, 2014, **111**(10), 2019–2026.
21 W. Yang, B. Hellner and F. Baneyx, Self-Immobilization of Car9 Fusion Proteins within High Surface Area Silica Sol-Gels and Dynamic Control of Protein Release, *Bioconjugate Chem.*, 2016, **27**(10), 2450–2459.
22 B. Hellner, S. B. Lee, A. Subramaniam, V. R. Subramanian and F. Baneyx, Modeling the Cooperative Adsorption of Solid-Binding Proteins on Silica: Molecular Insights from Surface Plasmon Resonance Measurements, *Langmuir*, 2019, **35**(14), 5013–5020.
23 B. Hellner, S. Alamdari, H. Pyles, S. Zhang, A. Prakash and K. G. Sprenger, *et al.*, Sequence-Structure-Binding Relationships Reveal Adhesion Behavior of the Car9 Solid-Binding Peptide: An Integrated Experimental and Simulation Study, *J. Am. Chem. Soc.*, 2020, **142**(5), 2355–2363.
24 B. L. Coyle and F. Baneyx, Direct and reversible immobilization and microcontact printing of functional proteins on glass using a genetically appended silica-binding tag, *Chem. Commun.*, 2016, **52**(43), 7001–7004.
25 J. Ma, B. Cai, S. Zhang, T. Jian, J. J. de Yoreo and C. L. Chen, *et al.*, Nanoparticle-mediated assembly of peptoid nanosheets functionalized with solid-binding proteins: designing heterostructures for hierarchy, *Nano Lett.*, 2021, **21**(4), 1636–1642.
26 X. Qi, Y. Zhao, K. Lachowski, J. Boese, Y. Cai and O. Dollar, *et al.*, Predictive Theoretical Framework for Dynamic Control of Bioinspired Hybrid Nanoparticle Self-Assembly, *ACS Nano*, 2022, **16**(2), 1919–1928.
27 J. Ma, B. Jin, K. N. Guye, M. E. Chowdhury, N. Y. Naser and C. L. Chen, *et al.*, Controlling Mineralization with Protein-Functionalized Peptoid Nanotubes, *Adv. Mater.*, 2023, **35**(3), 2207543.
28 Y. Cai, X. Qi, J. Boese, Y. Zhao, B. Hellner and J. Chun, *et al.*, Towards predictive control of reversible nanoparticle assembly with solid-binding proteins, *Soft Matter*, 2024, **20**(8), 1935–1942.
29 R. R. Naik, L. L. Brott, S. J. Clarson and M. O. Stone, Silica-Precipitating Peptides Isolated from a Combinatorial Phage Display Peptide Library, *J. Nanosci. Nanotechnol.*, 2002, **2**(1), 95–100.
30 B. Zhao, N. K. Li, Y. G. Yingling and C. K. Hall, LCST Behavior is Manifested in a Single Molecule: Elastin-Like polypeptide (VPGVG)$_n$, *Biomacromolecules*, 2016, **17**(1), 111–118.
31 D. E. Meyer and A. Chilkoti, Purification of recombinant proteins by fusion with thermally-responsive polypeptides, *Nat. Biotechnol.*, 1999, **17**(11), 1112–1115, DOI: **10.1038/15100**.
32 D. E. Meyer and A. Chilkoti, Quantification of the effects of chain length and concentration on the thermal behavior of elastin-like polypeptides, *Biomacromolecules*, 2004, **5**(3), 846–851.
33 Y. Cho, Y. Zhang, T. Christensen, L. B. Sagle, A. Chilkoti and P. S. Cremer, Effects of Hofmeister anions on the phase transition temperature of elastin-like polypeptides, *J. Phys. Chem. B*, 2008, **112**(44), 13765–13771.
34 F. G. Quiroz and A. Chilkoti, Sequence heuristics to encode phase behaviour in intrinsically disordered protein polymers, *Nat. Mater.*, 2015, **14**(11), 1164–1171.
35 C. E. Mills, E. Ding and B. D. Olsen, Cononsolvency of Elastin-like Polypeptides in Water/Alcohol Solutions, *Biomacromolecules*, 2019, **20**(6), 2167–2173.

36 K. Trabbic-Carlson, D. E. Meyer, L. Liu, R. Piervincenzi, N. Nath and T. LaBean, *et al.*, Effect of protein fusion on the transition temperature of an environmentally responsive elastin-like polypeptide: a role for surface hydrophobicity?, *Protein Eng., Des. Sel.*, 2004, **17**(1), 57–66.

37 A. K. Varanko, J. C. Su and A. Chilkoti, Elastin-Like Polypeptides for Biomedical Applications, *Annu. Rev. Biomed. Eng.*, 2020, **22**, 343–369, DOI: 10.1146/annurev-bioeng-092419-.

38 J. C. Rodríguez-Cabello, F. J. Arias, M. A. Rodrigo and A. Girotti, Elastin-like polypeptides in drug delivery, *Adv. Drug Delivery Rev.*, 2016, **97**, 85–100. Available from: https://www.sciencedirect.com/science/article/pii/S0169409X15300016.

39 S. R. MacEwan and A. Chilkoti, Elastin-like polypeptides: Biomedical applications of tunable biopolymers, *Pept. Sci.*, 2010, **94**(1), 60–77, DOI: 10.1002/bip.21327.

40 J. R. Simon, N. J. Carroll, M. Rubinstein, A. Chilkoti and G. P. López, Programming molecular self-assembly of intrinsically disordered proteins containing sequences of low complexity, *Nat. Chem.*, 2017, **9**(6), 509–515.

41 L. Li, N. K. Li, Q. Tu, O. Im, C. K. Mo and W. Han, *et al.*, Functional Modification of Silica through Enhanced Adsorption of Elastin-Like Polypeptide Block Copolymers, *Biomacromolecules*, 2018, **19**(2), 298–306.

42 N. Alvisi, F. A. Gutiérrez-Mejía, M. Lokker, Y. T. Lin, A. M. De Jong and F. Van Delft, *et al.*, Self-assembly of elastin-like polypeptide brushes on silica surfaces and nanoparticles, *Biomacromolecules*, 2021, **22**(5), 1966–1979.

43 S. Saha, S. Banskota, S. Roberts, N. Kirmani and A. Chilkoti, Engineering the Architecture of Elastin-Like Polypeptides: From Unimers to Hierarchical Self-Assembly, *Adv. Ther.*, 2020, **3**(3), 1900164.

44 W. Han, S. R. MacEwan, A. Chilkoti and G. P. López, Bio-inspired synthesis of hybrid silica nanoparticles templated from elastin-like polypeptide micelles, *Nanoscale*, 2015, **7**(28), 12038–12044.

45 Y. Qiu, Y. Lin and G. Zhang, Unique silica biomimetic mineralization of acidic elastin-like polypeptides without hydroxyl and charged residues, *Int. J. Biol. Macromol.*, 2020, **153**, 224–231.

46 N. J. Anthis and G. M. Clore, Sequence-specific determination of protein and peptide concentrations by absorbance at 205 nm, *Protein Sci.*, 2013, **22**(6), 851–858.

47 J. Skov Pedersen, Form factors of block copolymer micelles with spherical, ellipsoidal and cylindrical cores, *J. Appl. Crystallogr.*, 2000, **33**, 637–640.

48 K. Larson-Smith, A. Jackson and D. C. Pozzo, Small angle scattering model for Pickering emulsions and raspberry particles, *J. Colloid Interface Sci.*, 2010, **343**(1), 36–41. Available from: https://www.sciencedirect.com/science/article/pii/S0021979709014787.

49 D. Nečas and P. Klapetek, Gwyddion: an open-source software for SPM data analysis, *Cent. Eur. J. Phys.*, 2012, **10**(1), 181–188, DOI: 10.2478/s11534-011-0096-2.

50 J. Rao, Z. Luo, Z. Ge, H. Liu and S. Liu, 'Schizophrenic' micellization associated with coil-to-helix transitions based on polypeptide hybrid double hydrophilic rod-coil diblock copolymer, *Biomacromolecules*, 2007, **8**(12), 3871–3878.

51 C. Cai, W. Zhu, T. Chen, J. Lin and X. Tian, Synthesis and Self-assembly behavior of amphiphilic polypeptide-based brush-coil block copolymers, *J. Polym. Sci., Part A: Polym. Chem.*, 2009, **47**(22), 5967–5978.

52 M. Karg, T. Hellweg and P. Mulvaney, Self-assembly of tunable nanocrystal superlattices using poly-(NIPAM) spacers, *Adv. Funct. Mater.*, 2011, **21**(24), 4668–4676.

53 W. Zhu, J. Lin and C. Cai, The effect of a thermo-responsive polypeptide-based copolymer on the mineralization of calcium carbonate, *J. Mater. Chem.*, 2012, **22**(9), 3939–3947.

54 C. Cai, Y. Li, J. Lin, L. Wang, S. Lin and X. S. Wang, *et al.*, Simulation-assisted self-assembly of multicomponent polymers into hierarchical assemblies with varied morphologies, *Angew. Chem., Int. Ed.*, 2013, **52**(30), 7732–7736.

55 C. Cai, J. Lin, T. Chen, X. S. Wang and S. Lin, Super-helices self-assembled from a binary system of amphiphilic polypeptide block copolymers and polypeptide homopolymers, *Chem. Commun.*, 2009, (19), 2709–2711, DOI: 10.1039/B823367E.

56 E. Garanger, S. R. MacEwan, O. Sandre, A. Brûlet, L. Bataille and A. Chilkoti, *et al.*, Structural Evolution of a Stimulus-Responsive Diblock Polypeptide Micelle by Temperature Tunable Compaction of its Core, *Macromolecules*, 2015, **48**(18), 6617–6627.

57 K. Widder, S. R. MacEwan, E. Garanger, V. Núñez, S. Lecommandoux and A. Chilkoti, *et al.*, Characterisation of hydration and nanophase separation during the temperature response in hydrophobic/hydrophilic elastin-like polypeptide (ELP) diblock copolymers, *Soft Matter*, 2017, **13**(9), 1816–1822.

58 S. R. MacEwan, I. Weitzhandler, I. Hoffmann, J. Genzer, M. Gradzielski and A. Chilkoti, Phase Behavior and Self-Assembly of Perfectly Sequence-Defined and Monodisperse Multiblock Copolypeptides, *Biomacromolecules*, 2017, **18**(2), 599–609.

59 W. Hassouneh, E. B. Zhulina, A. Chilkoti and M. Rubinstein, Elastin-like Polypeptide Diblock Copolymers Self-Assemble into Weak Micelles, *Macromolecules*, 2015, **48**(12), 4183–4195.

60 J. W. Choi, S. H. Choi and J. I. Won, Self-Assembly Behavior of Elastin-like Polypeptide Diblock Copolymers Containing a Charged Moiety, *Biomacromolecules*, 2021, **22**(6), 2604–2613.

61 M. R. Dreher, A. J. Simnick, K. Fischer, R. J. Smith, A. Patel and M. Schmidt, *et al.*, Temperature triggered self-assembly of polypeptides into multivalent spherical micelles, *J. Am. Chem. Soc.*, 2008, **130**(2), 687–694.

62 B. Sharma, Y. Ma, A. L. Ferguson and A. P. Liu, In search of a novel chassis material for synthetic cells: emergence of synthetic peptide compartment, *Soft Matter*, 2020, **16**(48), 10769–10780, DOI: 10.1039/D0SM01644F.

63 S. Roberts, M. Dzuricky and A. Chilkoti, Elastin-like polypeptides as models of intrinsically disordered proteins, *FEBS Lett.*, 2015, **589**(19PartA), 2477–2486, DOI: 10.1016/j.febslet.2015.08.029.

64 V. Receveur-Bréchot and D. Durand, How Random are Intrinsically Disordered Proteins? A Small Angle Scattering Perspective, *Curr. Protein Pept. Sci.*, 2012, **13**, 55–75.

65 A. G. Kikhney and D. I. Svergun, A practical guide to small angle X-ray scattering (SAXS) of flexible and intrinsically disordered proteins, *FEBS Lett.*, 2015, **589**(19PartA), 2570–2577, DOI: **10.1016/j.febslet.2015.08.027**.

66 J. C. Berg, *An Introduction to Interfaces & Colloids: The Bridge to Nanoscience*, World Scientific, 2010.

67 K. M. Roth, Y. Zhou, W. Yang and D. E. Morse, Bifunctional small molecules are biomimetic catalysts for silica synthesis at neutral pH, *J. Am. Chem. Soc.*, 2005, **127**(1), 325–330.

68 Y. Cai, N. Y. Naser, J. Ma and F. Baneyx, Precision Loading and Delivery of Molecular Cargo by Size-Controlled Coacervation of Gold Nanoparticles Functionalized with Elastin-like Peptides, *Biomacromolecules*, 2024, **25**(4), 2390–2398.

69 N. P. Shusharina, I. A. Nyrkova and A. R. Khokhlov, Diblock Copolymers with a Charged Block in a Selective Solvent: Micellar Structure, *Macromolecules*, 1996, **29**(9), 3167–3174, DOI: **10.1021/ma9515745**.

70 J. F. Marko and Y. Rabin, Microphase separation of charged diblock copolymers: melts and solutions, *Macromolecules*, 1992, **25**(5), 1503–1509, DOI: **10.1021/ma00031a022**.

71 S. Xi, L. Wang, J. Liu and W. Chapman, Thermodynamics, Microstructures, and Solubilization of Block Copolymer Micelles by Density Functional Theory, *Langmuir*, 2019, **35**(14), 5081–5092.

72 P. Hervé, M. Destarac, J. F. Berret, J. Lal, J. Oberdisse and I. Grillo, Novel core-shell structure for colloids made of neutral/polyelectrolyte diblock copolymers and oppositely charged surfactants, *Europhys. Lett.*, 2002, **58**(6), 912–918. Available from: **https://iopscience.iop.org/article/10.1209/epl/i2002-00104-y**.

73 Y. Lu, J. Lin, L. Wang, L. Zhang and C. Cai, Self-Assembly of Copolymer Micelles: Higher-Level Assembly for Constructing Hierarchical Structure, *Chem. Rev.*, 2020, **120**, 4111–4140.

74 S. Jain and F. S. Bates, On the Origins of Morphological Complexity in Block Copolymer Surfactants, *Science*, 2003, **300**(5618), 460–464, DOI: **10.1126/science.1082193**.

75 M. B. Van Eldijk, F. C. M. Smits, N. Vermue, M. F. Debets, S. Schoffelen and J. C. M. Van Hest, Synthesis and self-assembly of well-defined elastin-like polypeptide-poly(ethylene glycol) conjugates, *Biomacromolecules*, 2014, **15**(7), 2751–2759.

76 I. Weitzhandler, M. Dzuricky, I. Hoffmann, F. Garcia Quiroz, M. Gradzielski and A. Chilkoti, Micellar Self-Assembly of Recombinant Resilin-/Elastin-Like Block Copolypeptides, *Biomacromolecules*, 2017, **18**(8), 2419–2426.

77 T. Coradin and J. Livage, Effect of some amino acids and peptides on silicic acid polymerization, *Colloids Surf., B*, 2001, **21**(4), 329–336.

78 T. Coradin and P. J. Lopez, Biogenic silica patterning: Simple chemistry or subtle biology?, *ChemBioChem*, 2003, **4**(4), 251–259.

79 S. J. Roeters, R. Mertig, H. Lutz, A. Roehrich, G. Drobny and T. Weidner, Backbone Structure of Diatom Silaffin Peptide R5 in Biosilica Determined by Combining Solid-State NMR with Theoretical Sum-Frequency Generation Spectra, *J. Phys. Chem. Lett.*, 2021, **12**(39), 9657–9661.

80 N. Kröger, S. Lorenz, E. Brunner and M. Sumper, Self-Assembly of Highly Phosphorylated Silaffins and Their Function in Biosilica Morphogenesis, *Science*, 2002, **298**(5593), 584–586, DOI: **10.1126/science.1076221**.

81 B. Hellner, A. E. Stegmann, K. Pushpavanam, M. J. Bailey and F. Baneyx, Phase Control of Nanocrystalline Inclusions in Bioprecipitated Titania with a Panel of Mutant Silica-Binding Proteins, *Langmuir*, 2020, **36**(29), 8503–8510.

82 M. Pagliaro and G. J. Hutchings, Heterogeneous catalysis for fine chemicals, *Catal. Sci. Technol.*, 2011, **1**(9), 1543, DOI: **10.1039/C1CY90035H**.

83 J. Shi, On the Synergetic Catalytic Effect in Heterogeneous Nanocomposite Catalysts, *Chem. Rev.*, 2013, **113**(3), 2139–2181, DOI: **10.1021/cr3002752**.

84 C. H. Lee, L. W. Lo, C. Y. Mou and C. S. Yang, Synthesis and characterization of positive-charge functionalized mesoporous silica nanoparticles for oral drug delivery of an anti-inflammatory drug, *Adv. Funct. Mater.*, 2008, **18**(20), 3283–3292.

85 M. H. Kim, H. K. Na, Y. K. Kim, S. R. Ryoo, H. S. Cho and K. E. Lee, *et al.*, Facile synthesis of monodispersed mesoporous silica nanoparticles with ultralarge pores and their application in gene delivery, *ACS Nano*, 2011, **5**(5), 3568–3576.

86 M. Vallet-Regí, L. Ruiz-González, I. Izquierdo-Barba and J. M. González-Calbet, Revisiting silica based ordered mesoporous materials: medical applications, *J. Mater. Chem.*, 2006, **16**(1), 26–31, DOI: **10.1039/B509744D**.

87 H. Kang, D. J. Long and C. L. Haynes, Preparation of Colloidally Stable Positively Charged Hollow Silica Nanoparticles: Effect of Minimizing Hydrolysis on ζ Potentials, *Langmuir*, 2019, **35**(24), 7985–7994.

88 J. Lee, C. K. Hong, S. Choe and S. E. Shim, Synthesis of polystyrene/silica composite particles by soap-free emulsion polymerization using positively charged colloidal silica, *J. Colloid Interface Sci.*, 2007, **310**(1), 112–120. Available from: **https://www.sciencedirect.com/science/article/pii/S0021979706010411**.

89 C. Clavero, Plasmon-induced hot-electron generation at nanoparticle/metal-oxide interfaces for photovoltaic and photocatalytic devices, *Nat. Photonics*, 2014, **8**(2), 95–103.

90 H. Veisi, P. Abassi, P. Mohammadi, T. Tamoradi and B. Karmakar, Gold nanoparticles decorated biguanidine modified mesoporous silica KIT-5 as recoverable heterogeneous catalyst for the reductive degradation of environmental contaminants, *Sci. Rep.*, 2021, **11**(1), 2734.

91 S. Rasouli, S. Davaran, F. Rasouli, M. Mahkam and R. Salehi, Positively charged functionalized silica nanoparticles as nontoxic carriers for triggered anticancer drug release, *Des. Monomers Polym.*, 2014, **17**(3), 227–237, DOI: **10.1080/15685551.2013.840475**.

92 I. H. Yoon, S. B. Yoon, Y. Sihn, M. S. Choi, C. H. Jung and W. K. Choi, Stabilizing decontamination foam using surface-modified silica nanoparticles containing chemical reagent: foam stability, structures, and dispersion properties, *RSC Adv.*, 2021, **11**(3), 1841–1849, DOI: **10.1039/D0RA07644A**.

93 M. T. Bore, H. N. Pham, E. E. Switzer, T. L. Ward, A. Fukuoka and A. K. Datye, The Role of Pore Size and Structure on the Thermal Stability of Gold Nanoparticles

within Mesoporous Silica, *J. Phys. Chem. B*, 2005, **109**(7), 2873–2880, DOI: **10.1021/jp045917p**.

94 Y. S. Chi, H. P. Lin and C. Y. Mou, CO oxidation over gold nanocatalyst confined in mesoporous silica, *Appl. Catal., A*, 2005, **284**(1), 199–206. Available from: **https://www.sciencedirect.com/science/article/pii/S0926860X05000670**.

95 L. H. Ren, H. L. Zhang, A. H. Lu, Y. Hao and W. C. Li, Porous silica as supports for controlled fabrication of $Au/CeO_2/SiO_2$ catalysts for CO oxidation: Influence of the silica nanostructures, *Microporous Mesoporous Mater.*, 2012, **158**, 7–12. Available from: **https://www.sciencedirect.com/science/article/pii/S1387181112001503**.

96 X. Yu and C. T. Williams, Recent advances in the applications of mesoporous silica in heterogeneous catalysis, *Catal. Sci. Technol.*, 2022, **12**(19), 5765–5794, DOI: **10.1039/D2CY00001F**.